Highlights

A stress- and strain-dependent constitutive modelling of the large-scale in situ PRACLAY heater test

Hangbiao Song, Arnaud Dizier, Séverine Levasseur, Suresh Seetharam, Frédéric Collin

- A large-scale in situ PRACLAY heater test to investigate the thermal pressurization in the near field and to verify the far field performance.
- An advanced constitutive model integrating both the stress and strain dependency of the intrinsic permeability and clay stiffness.
- Triaxial test modelling from the in situ extraction of the sample to the laboratory test to validate the capability of the advanced constitutive model.

A stress- and strain-dependent constitutive modelling of the large-scale in situ PRACLAY heater test

Hangbiao Song[a], Arnaud Dizier[b], Séverine Levasseur[c], Suresh Seetharam[b], Frédéric Collin[a]

[a] *Urban and Environmental Engineering Research Unit, Université de Liège, 9 Allée de la Découverte, Liège, 4000, Belgium*
[b] *European Underground Research Infrastructure for Disposal of Nuclear Waste in Clay Environment, EURIDICE, 200 Boeretang, Mol, 2400, Belgium*
[c] *ONDRAF/NIRAS, Avenue des Arts 14, Bruxelles, 1210, Belgium*

Abstract

In Belgium, Boom Clay is considered as a potential geological formation for the disposal of radioactive waste in deep geological layer. The design and the long term safety of such underground facilities require the in situ thermo-hydro-mechanical (THM) characterization of the host geological formation. In particular, the potential impact of temperature elevation both on the excavation damage zone (EDZ, near field) and on the intact rock/clay formation (far field) has to be studied. The laboratory tests and small scale in situ heater tests on Boom Clay showed the strong THM coupling behavior but these experiments suffered the inevitable disturbance and low accuracy due to the small scale. The large-scale in situ PRACLAY heater test, conducted in the HADES underground research laboratories (URL) (Mol, Belgium), aims at filling this gap by heating the Boom Clay at large scale to reproduce the thermal impacts in the EDZ (or the near field) and to verify at large scale the far field performance. A 2D benchmark exercise within the framework of the European Joint programme EURAD HITEC has been proposed to model the PRACLAY heater test with fully coupled THM finite element code and to investigate the in situ behavior of the host clay formation. The thermal pressurization due to the discrepancy of thermal expansion between the fluid and solid skeleton is well predicted. To well reproduce the evolution of pore water pressure, the strain dependency of the intrinsic permeability and the stress dependency of the Young's modulus are considered in the advanced modelling. The small strain stiffness theory of the HSsmall model is also taken into account. The constitutive model is used to reproduce the sample extraction from the host medium and then the triaxial test. The results evidence the capability of the model to predict Young's modulus measured in the laboratory. Finally, a good agreement is observed between the in situ measurements and the numerical results. The benchmark provides valuable insights into the THM impact on the host rock/clay formation and reliable indications on the model capacity.

Keywords: PRACLAY heater test, Boom Clay, THM modelling, clay stiffness, permeability

---

1. Introduction

In every nuclear power-producing country, the long-term management of high-level and heat-emitting radioactive wastes is an important environmental concern (IAEA, 2022). Deep geological disposal is widely considered as one of the most sustainable solutions for isolating radioactive waste from the biosphere and ensuring its long-term management (Bredehoeft, 1978; IAEA, 2003). The general idea of geological disposal in clay (or clayrock) formation is to dispose the radioactive waste inside a geological formation with favorable properties such as its low permeability, self-sealing properties, and capacity of retention of radionuclides at the surface of the clay materials (Félix et al., 1996; Neerdael and Boyazis, 1997; Croisé et al., 2004; Bernier et al., 2007).

However, high-level radioactive waste emits a significant amount of heat, which leads to elevated temperature over 70 °C in the geological host formation (Collin et al., 2002; Gens Solé et al., 2020; Dizier et al., 2021; Li et al., 2023a). Thus, it is important to study the perturbation resulting from the thermal effects and the potential impact on the favorable characteristics, such as its transport capabilities, of the host rock/clay formation (Bossart et al., 2002). In addition, when the pore water expands thermally, excess pore pressure may cause the formation of new fractures or the reactivation and propagation of old ones in the near field, altering the permeability (Gens et al., 2011). Tensile or shear failure could be induced at the halfway zone between two adjacent cells in the far field, where the thermal load is applied to the host rock/clay formation from both sides (Braun et al., 2022). Old fractures/faults could be also reactivated based on the distance between two neighboring cells and the thermal load intensity (Plúa et al., 2021). Understanding the thermo-hydro-mechanical (THM) behavior of the host rock/clay formation is thus an important input for the design of a geological radioactive waste disposal, to prevent the formation of the above fractures and failures. Some underground research laboratories (URL) have already developed in situ heater tests to examine how temperature affects the THM behavior of host rock/clay formation. Examples of these tests include the HE-D test and the FE experiment in Switzerland conducted in the Mont Terri URL (Garitte et al., 2017; Müller et al., 2018), the TED, CRQ, EPT, ALC1604 and ALC1605 tests in France conducted in the Meuse/Haute-Marne URL (Armand et al., 2017; Seyedi et al., 2021; Conil et al., 2020; Bumbieler et al., 2021).

In Belgium, a poorly indurated clay named Boom Clay is considered as a potential host clay formation thanks to its low intrinsic permeability, its excellent self-sealing property, and its capability of adsorption of radionuclides (Bernier et al., 2007; Sultan et al., 2010). As a marine Oligocene deposit, Boom Clay is mostly located in northern Belgium and has a moderate dip (around 1°) towards the north and east. It has an average thickness of 100 meters in the Mol region (Mertens et al., 2004). In 1974, the Belgian Nuclear Research Center (SCK-CEN) initiated a research, development, and demonstration programme (RD&D) for the underground disposal of radioactive waste (Li et al., 2023b). The HADES URL was constructed in the 1980s, at a depth of 190 to 290 meters beneath the surface of SCK-CEN, near the center of the Boom Clay formation. RD&D programme has been conducted for more than 40 years, to evaluate how temperature affects the characteristics and behavior of Boom Clay. Laboratory tests (Baldi et al., 1988; Sultan et al., 2002; Delage et al., 2000; Cui et al., 2000, 2009; Li et al., 2023a) and in situ small scale heater tests (BACCHUS, CACTUS, CERBERUS, and ATLAS experiments) realized in the HADES URL already showed the strong THM coupled behavior of Boom Clay (De Bruyn and Labat, 2002; Chen et al., 2011; Bernier and Neerdael, 1996; Dao et al., 2015; Li et al., 2023a). However, on the one hand, the relatively limited size of these tests suffers from the inevitable mechanical disturbance induced by the installation of the heater and a lower accuracy in reproducing the thermal pressurization in the excavation damaged zone (EDZ) (Chen et al., 2021a). On the other hand, the distance between the monitoring points and the heater setup is believed to be sufficiently large for the clay to be assumed undisturbed at the location of the sensors. This only allows the characterization of the far-field Boom Clay THM behavior. To fully understand the Boom Clay THM behavior in near-field galleries, these interpretative heater tests are therefore not sufficient.

To address this knowledge gap and provide insight into how temperature affects the EDZ in the Boom Clay, a large-scale in situ PRACLAY heater test has been built and is currently being conducted in the HADES URL (Li et al., 2010). The large-scale PRACLAY heater test intends to investigate the combined effect of the large-scale thermal load caused by the high-level radioactive waste decay in deep Boom Clay formation and the hydro-mechanical disturbances resulting from the excavation of the gallery. It will allow to test whether or not the clay can withstand temperature increases in the near field (or in the EDZ), and in the far field without losing any of its advantageous properties for the radioactive waste geological disposal.

The ongoing large-scale PRACLAY heater test started in November 2014, further information regarding its design, experimental setup, and first observation derived from the monitoring system can be obtained in Dizier et al. (2021). This study focuses on the in situ characterization of THM behavior of Boom Clay at full scale, to verify the accuracy and capability of our numerical modelling. After a short description of the experimental test in section 2, a benchmark exercise on the PRACLAY heater test is introduced with the constitutive model and material properties. The preliminary numerical prediction of the benchmark is displayed in section 3, where the overpressure induced by thermal pressurization is theoretically analyzed. To better reproduce the experimental observations, an advanced constitutive modelling is introduced by integrating the dependency of both the intrinsic permeability and the clay stiffness on the mean effective stress and shear strain in section 4. A triaxial test modelling is proposed to model the sample extraction from the in situ to the laboratory test, to verify the capability of the model. Finally, a good agreement is observed between the in situ measurements and the numerical results.

2. Large-scale in situ PRACLAY heater test

2.1. Introduction to the large-scale in situ PRACLAY heater test

A large-scale in situ PRACLAY heater test is being carried out by EURIDICE in the HADES URL in Mol within the framework of RD&D programme on radioactive waste geological disposal in Belgium. The main goal of the experiment is to study the combined effect of the thermal loading and the hydro-mechanical disturbances induced by the gallery excavation. Another objective is to validate the large-scale thermal characteristics of Boom

Clay, based on previous estimates from the small-scale in situ ATLAS experiment (Chen et al., 2011; De Bruyn and Labat, 2002; Li et al., 2023a).

The HADES URL was built at a depth of approximately 225 m in the Boom Clay Formation and its construction was realized in different steps starting from the beginning of the eighties to the construction of the PRACLAY gallery (PG) in 2007 (Li et al., 2023b) (Fig. 1).

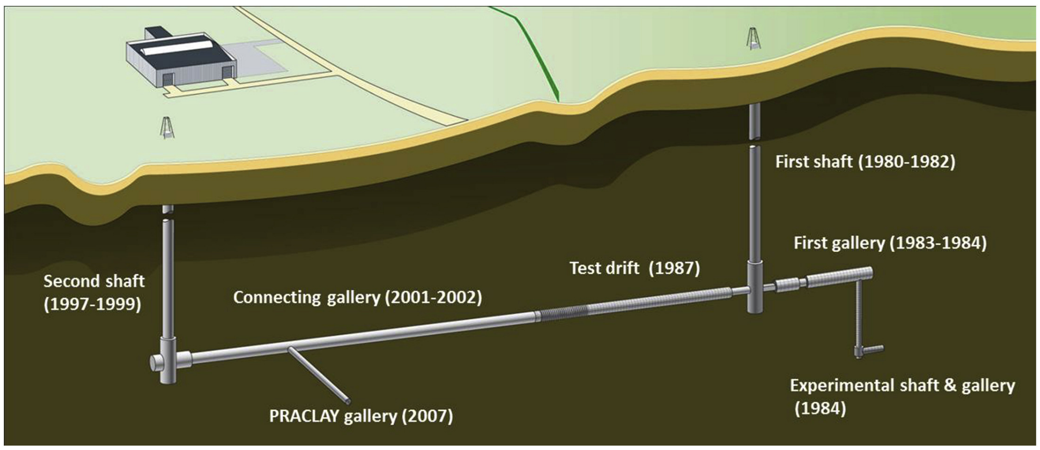

Figure 1: Layout of the underground laboratory at Mol, Belgium (EURIDICE website, 2018).

2.2. *Experimental set-up and main steps of the PRACLAY heater test*

The PG was constructed perpendicularly to the Connecting gallery from October 4, 2007 to November 6, 2007. Fig. 2 shows the overview of the experimental setup of the PRACLAY heater test, and a short introduction about the geometry and materials of the test setup is here presented. More information is available in Van Marcke et al. (2013). With a length of 45 m and an external diameter of 2.5 m, the gallery is lined by 81 concrete lining rings (Ring 1-Ring 81) with a thickness of 0.3 m and a length of 0.5 m. Most of the rings possess a concrete grade of C80/95. Each ring primarily comprises of 8 regular segments (S1-S8) and a single key segment S9. At the end of the PG, C30/37 concrete was poured over a length of 2 m to form the end plug. The diameter of this plug is slightly larger than the rest of the gallery. The steel structure of the tunneling shield, made in carbon steel, was left in place supporting the 2.5 m-long gallery between the end plug and the last ring.

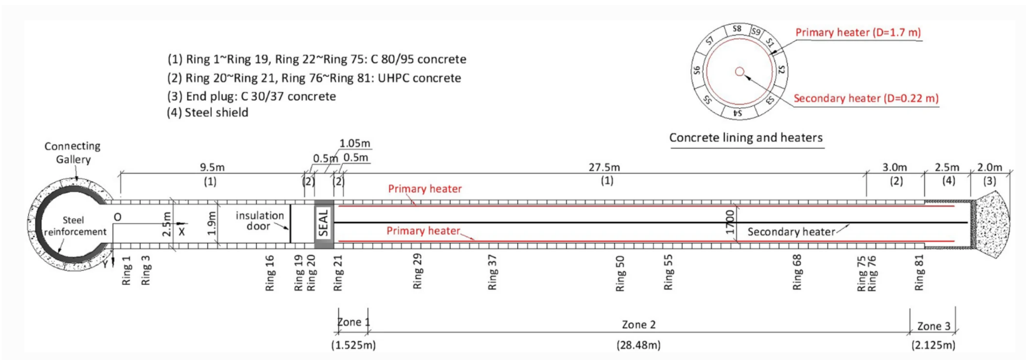

Figure 2: Overview of the PG and experimental setup (Chen et al., 2021a).

A 1.05 m-long hydraulic bentonite-based seal was installed between Ring 20 and Ring 21 to create a hydraulic cut-off between the heated and the non-heated part of the PG. It was installed from January 18, 2010 to February 11, 2010. The hydraulic seal is constructed of massive stainless steel (downstream flange, upstream flange, steel cylinder, closing steel frame) and compacted MX-80 bentonite blocks placed against Boom Clay in external annular rings.

The heater system is composed of two main systems. The first one, the primary heater consists of electric cables placed 100 mm from the gallery intrados. The second one, which is a back-up one, was placed at the center of the gallery and will work only if the primary system fails. To achieve the expected boundary conditions and to maximize the heat transfer from the heater elements to the concrete lining, backfilling with M34 Mol sand was done in the heated section of the PG in 2011. This operation was realized by blowing it into the gallery in a dry state and was then artificially pressurized. From January to May 2012, a total volume of about 43 m^3 was injected into this section of the gallery, and a five-step artificial increase in pore water pressure, as seen in Fig. 3, was carried out. A natural saturation of the backfilled gallery was achieved by the water flowing into it from the adjacent Boom Clay. At the commencement of heating experiment, the pore water pressure pointed to 1 MPa. The pressure in the experiment naturally changes during the heating period without human intervention (adding or removing water).

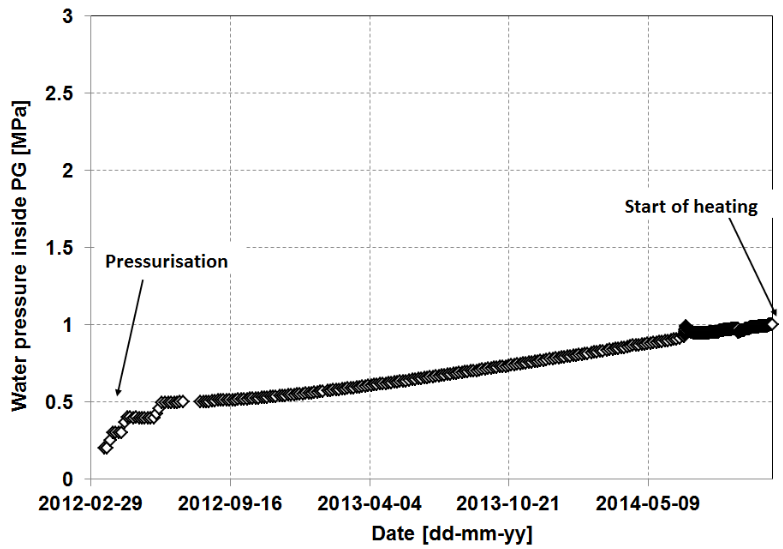

Figure 3: Evolution of the pore water pressure inside the backfilled part of the PG before the switch-on of the heater (Dizier et al., 2016).

On November 3, 2014, upon activation of the primary heater, the power of the heater was stepwise increased until the temperature of the lining extrados pointed to 80 °C. The first phase is called the start-up heating phase (Dizier et al., 2016). Thereafter, the heater power was reduced step by step to keep the temperature of the lining extrados at 80 °C. This phase is called the stationary heating phase lasting 10 years from August 2015 to August 2025 (Dizier et al., 2016). In March 2015, a door was installed in front of the seal to provide insulation to limit as much as possible the dissipation of heat through the non-heated section.

A large instrumentation network with approximately 1100 sensors was installed around the PG to monitor and follow up the responses in the test setup and the Boom Clay formation. Boreholes drilled from Connecting Gallery (CG boreholes) and PG (PG boreholes) were equipped with multi-filter piezometers complemented with thermocouples. Fig. 4 presents the 3D view of the monitoring boreholes surrounding the PG. However, the experimental results discussed herein are limited to the vertical borehole PG50D and the horizontal boreholes CG35E, CG38E, CG42E and CG49E. The CG boreholes are positioned in the horizontal plane, which contains both the PG and the Connecting Gallery, while the PG50D borehole is oriented in the vertical direction, perpendicular to this horizontal plane. The locations of the sensors in the horizontal and vertical directions of a plane located at the middle of the heated section are illustrated in Tab. 1. The X and Y axes correspond to the coordinate system shown in Fig. 5 in section 3.1, with the origin defined at point O.

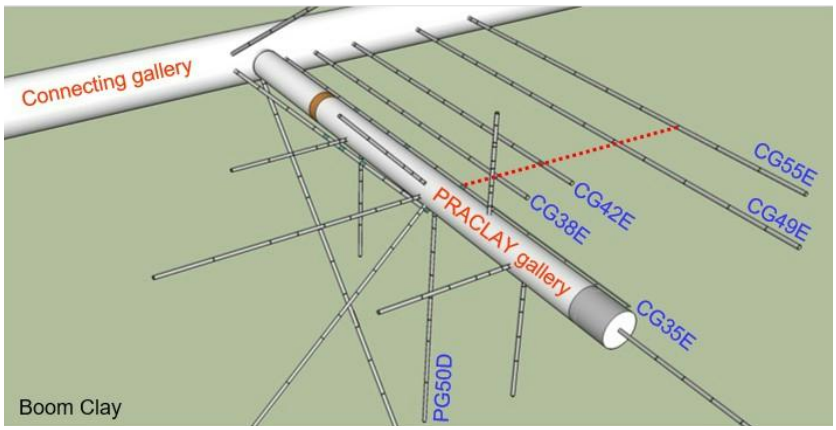

Figure 4: 3D view of the monitoring boreholes surrounding the PG (Chen et al., 2021a).

Table 1: Locations of the sensors in the horizontal plane and the vertical direction (Dizier et al., 2016).

	Sensors	Coordinates (X, Y)
Horizontal plane	Interface "B"	(1.31, 0)
	CG35E-6	(2.23, 0.14)
	CG38E-2	(4.69, 0.24)
	CG42E-2	(8.97, 0.04)
	CG49E-5	(16.14, 0.32)
Vertical direction	Interface "F"	(0, 1.31)
	PG50D-10	(0.03, 1.49)
	PG50D-9	(0.03, 1.99)
	PG50D-8	(0.03, 2.99)
	PG50D-7	(0.03, 4.99)
	PG50D-6	(0.03, 6.99)
	PG50D-5	(0.03, 8.99)
	PG50D-4	(0.02, 10.99)
	PG50D-3	(0.02, 12.99)
	PG50D-2	(0.02, 16.99)
	PG50D-1	(0.02, 20.99)

3. A benchmark exercise with PRACLAY heater test

3.1. Geometry and mesh

A two-dimensional (2D) plane strain benchmark within the framework of the European Joint programme (EURAD-HITEC, 2019), is proposed to model the PRACLAY heater test with fully coupled THM finite element code and to investigate the in situ behavior of the host clay formation. Two principal modelling cases are proposed in this exercise. The first one consists of an "academic version" of the PRACLAY heater test, where the main goal is to calibrate the numerical codes among different teams with relatively basic mechanical models. The second case corresponds to a "free version", where the modelling teams are free to choose the constitutive law. In all cases, it is proposed to model the experiment from the beginning of the excavation to the on-going running heater test. It is worth mentioning that, this paper mainly focuses on the free case to better reproduce the experimental observations from the in situ test.

The numerical prediction is carried out with the FEM code Lagamine developed at the University of Liège (Charlier, 1987). This model represents the midplane (around Ring 50) of the PRACLAY heater Test (which is perpendicular to the PG axis) in a middle cross-section of the heated gallery. Only a quarter of the full cross section is modelled due to the symmetry of the problem, and the simulated area is 100 m wide in both directions (Fig. 5). Due to the cross-anisotropy characteristic of Boom Clay, the horizontal direction is defined as parallel to the bedding plane for numerical simplification, while the vertical direction corresponds to the normal to the bedding. The discretized mesh consists of 18543 nodes and 6120 elements. Each element is a 2D isoparametric element with eight nodes, where displacement fields, fluid pressure, and temperature are interpolated. As shown in Fig. 5, the numerical model incorporates two materials: Boom Clay and concrete lining. The segmental concrete lining is modelled through a monolithic ring where the joints are not represented. The concrete lining has an inner radius of 0.95 m and an outer radius of 1.25 m, respectively. The excavation radius is estimated to be 1.31 m, with a 6 cm over-excavation being considered. It is worth noting that the backfilled sand is not considered in any modelling for simplification.

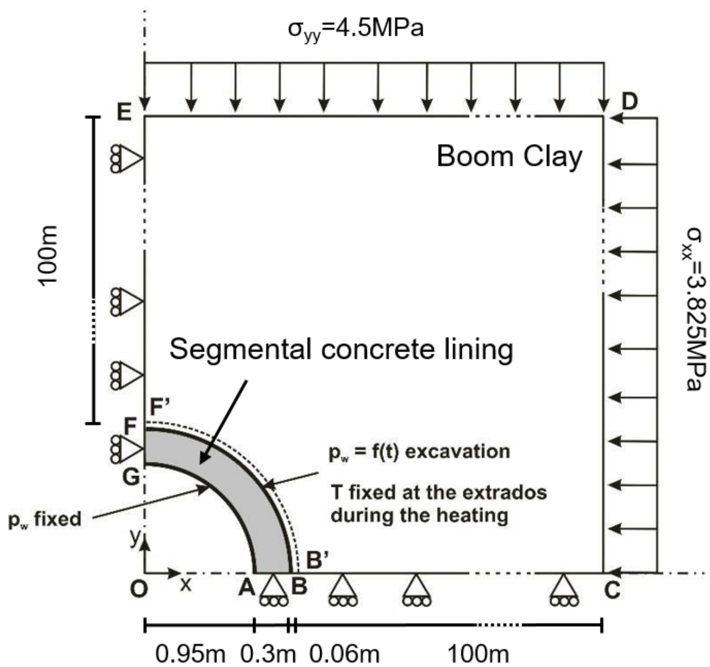

Figure 5: Geometry (not at scale) and materials for the PRACLAY heater test within the 2D plane strain coupled THM model.

The initial conditions for Boom Clay are presented in Tab. 2. These values come form the in situ measurements at the level of the URL and previous studies on Boom Clay (Bernier et al., 2007; Chen et al., 2011). A constant temperature of 16.5 °C is defined for all the materials initially. The initial pore pressure in the Boom Clay is 2.25 MPa, while an initial pore pressure of 0.1 MPa is assumed in the concrete. There is no initial stress defined for the lining. At the external boundary (CD and DE), constant total stress, pore pressure, and temperature are imposed during the full computation. Due to the symmetry conditions, the water and thermal flow along the symmetry axes are prevented by the introduction of an adiabatic and an impervious boundary. The normal displacements are fixed.

Table 2: Initial conditions for Boom Clay.

Parameters		Components	Boom Clay
		σ_{yy}	4.5
Total stress	MPa	σ_{xx}	3.825
		σ_{zz}	3.825
Pore pressure	MPa	P_0	2.25
Temperature	°C	T_0	16.5

The proposed model is conducted by adapting the boundary conditions of the gallery wall and concrete lining (Fig. 5). The main time points of the PRACLAY heater test are presented in Tab. 3, where t_0 denotes the start of excavation. For the mechanical boundary conditions, a stress release technique combined with contact elements is used to model the progressive contact between Boom Clay and concrete lining during gallery excavation. The total stress at the gallery wall is reduced to 0.1 MPa within 24 hours (t_0+1 day), after which it remains constant. In terms of the hydraulic boundary conditions, the pore pressure is reduced to 0.1 MPa during excavation (t_0+1 day). The model is allowed to stabilize before artificial pressurization, during which the pore pressure inside the gallery wall equals the atmospheric pressure (between t_0+1 day and t_0+1609 days). From the start of the artificial pressurization in the backfill sand up to the end of the heating phase (t_0+6522 days), the pore water pressure at the intrados of the lining (boundary GA) follows the in situ measurements, as shown in Fig. 6. Regarding thermal boundary conditions, the lining extrados is set with a temperature boundary condition derived from the in situ measurements, as depicted in Fig. 7. A stepwise heating phase with different heat power is described. The heater was switched on November 3, 2014 (t_0+2582 days), and a temperature of 80 °C was reached at the lining extrados on August 17, 2015 (t_0+2829 days). Hereafter the temperature was maintained at 80 °C for 10 years until August 17, 2025 (t_0+6522 days).

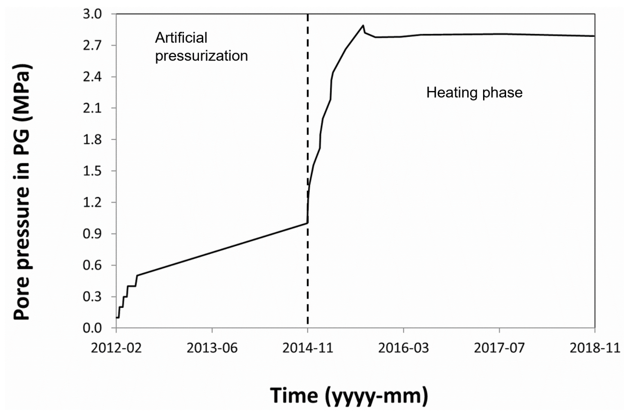

Figure 6: Pore pressure boundary condition in the PG after pressurization used in the 2D plain strain model, modified from Dizier et al. (2021).

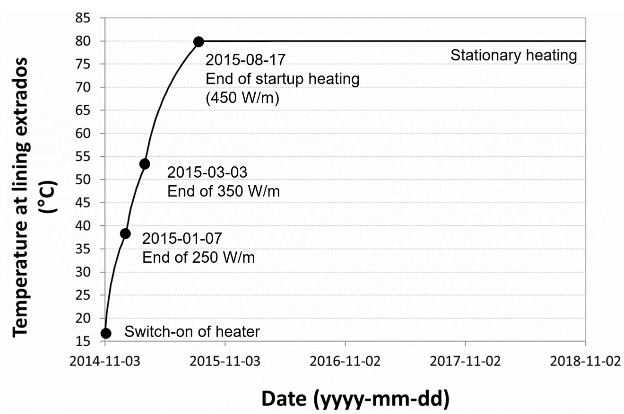

Figure 7: Temperature boundary condition at the lining extrados, modified from Dizier et al. (2021).

Table 3: Main time slots of the PRACLAY heater test.

Test phases	Date	Days (t_0+days)
End of excavation	2007-10-10	t_0+1
Before pressurization	2012-03-05	t_0+1609
Before switch-on of heater	2014-11-03	t_0+2582
End of 250 W/m	2015-01-07	t_0+2647
End of 350 W/m	2015-03-03	t_0+2702
End of startup heating	2015-08-17	t_0+2869
3 years heating	2018-08-17	t_0+3965
10 years heating	2025-08-17	t_0+6522

3.2. Balance equations

To numerically investigate the coupled THM problem in the PRACLAY heater test, it is essential to establish the governing balance equations. A fully saturated condition is assumed in the modelling. This assumption is supported by several factors. First, the excavation of the PG was carried out rapidly, followed by the immediate installation of the concrete liner. Hence the ventilation between the PG and the Connecting Gallery was limited. Second, the PG was backfilled with sand and subsequently subjected to artificial pressurization, which led to a rise in pore pressure, as shown in Fig. 3. Over time, the inflow of water from the surrounding Boom Clay resulted in the natural saturation of the backfilled gallery. As a result, the Boom Clay was considered fully saturated prior to the initiation of the heating phase. Consequently, any variations in saturation during excavation and heating are not accounted for in this study. Under these conditions, the porous medium is treated as a continuous mixture composed of a solid phase and a water phase. Some studies further classify the water phase into free and bound water components. The dehydration of bound water at elevated temperatures can contribute to pore pressure generation (Sojoudi and Li, 2023; Sojoudi et al., 2024). However, for the sake of simplicity, this effect is not considered in the present study. The governing equations for momentum, mass, and energy balance are established, with further details available in Song et al. (2023) and Simo et al. (2025).

The momentum balance equation accounts for both the effective stresses within the solid matrix and the external body forces acting on it and is expressed as follows:

$$\frac{\partial \sigma_{ij}}{\partial x_j} + G_i = 0 \tag{1}$$

where σ_{ij} is the total Cauchy stress tensor, x_j denotes the Cartesian coordinates. G_i is the body force per unit volume, typically associated with gravity.

The mass balance equations for the solid and water phases are formulated within the framework of classical poromechanics. The conservation of solid mass is expressed in its time derivative form as:

$$\dot{M}_s = \frac{\partial}{\partial t}\Big(\rho_s(1-\phi)\Omega\Big) = 0 \tag{2}$$

where ρ_s denotes the density of the solid phase, and $\phi = \Omega_v/\Omega$ is the porosity, defined as the ratio of pore volume Ω_v to the total material volume Ω.

The water mass balance equation is given by:

$$\frac{\partial f_{w,i}}{\partial x_i} + \dot{M}_w - Q_w = 0 \tag{3}$$

where $\dot{M}_w$ is the time derivative of the water mass, Q_w is a water source/sink term, and $f_{w,i}$ represents the water flux, governed by Darcy's law. Under fully saturated conditions, the mass of fluid in a representative elementary volume Ω is:

$$M_w = \rho_w \phi \Omega \tag{4}$$

where ρ_w denotes the fluid density. Taking the time derivative of the fluid mass per unit mixture volume yields:

$$\dot{M}_w = \rho_w\Big(\big(\frac{\dot{p}_w}{K_w} - \alpha_w \dot{T}\big)\phi - (1-\phi)\alpha_d \dot{T} + \frac{\dot{\Omega}}{\Omega}\Big) \tag{5}$$

where K_w is the bulk modulus of the fluid phase. α_d is the drained volumetric thermal expansion coefficient of the porous medium, and α_w is the temperature-dependent thermal expansion coefficient of the fluid (Kell, 1975). For a homogeneous, isotropic porous medium, α_d is typically taken as equal to the thermal expansion coefficient of the solid skeleton, $3\alpha_s$ (Ghabezloo et al., 2009).

The fluid flow is obtained by using the Darcy's law:

$$f_{w,i} = -\rho_w \frac{k_{ij}}{\mu_w}\Big(\frac{\partial p_w}{\partial x_j} + \rho_w g_j\Big) \tag{6}$$

where k_{ij} is the intrinsic permeability tensor, g_j is the gravity acceleration vector, and μ_w is the fluid viscosity which is considered temperature-dependent (Rumble, 2019).

The energy balance equation is achieved using classic poromechanics theory and written for a unit mixture volume:

$$\frac{\partial f_{T,i}}{\partial x_i} + \dot{S}_T - Q_T = 0 \tag{7}$$

where $\dot{S}_T$ is the time derivative of the enthalpy, $f_{T,i}$ is the thermal flow, and Q_T is the heat source/sink term. The total enthalpy S_T of the system is expressed as the sum of the contributions from both the fluid and solid phases:

$$S_T = \left(\phi\rho_w c_{p,w} + \left(1-\phi\right)\rho_s c_{p,s}\right)\left(T - T_0\right)\Omega \tag{8}$$

where $c_{p,w}$ and $c_{p,s}$ are the specific heat capacities of the fluid and solid phases, respectively, T_0 is the initial reference temperature. The time derivative of the enthalpy for a unit volume of the porous medium, which represents the rate of heat storage, can be written as:

$$\begin{aligned}\dot{S}_T = {} & c_{p,w}\rho_w\left(1-\phi\right)\left(\frac{\dot{\Omega}}{\Omega} - \alpha_d\dot{T}\right)\left(T-T_0\right) + c_{p,w}\rho_w\phi\left(\frac{\dot{p}_w}{K_w} - \alpha_w\dot{T}\right)\left(T-T_0\right) \\ & + c_{p,w}\rho_w\phi\dot{T} + c_{p,w}\rho_w\phi\left(T-T_0\right)\frac{\dot{\Omega}}{\Omega} + c_{p,s}\rho_s\left(1-\phi\right)\dot{T}\end{aligned} \tag{9}$$

The thermal flow $f_{T,i}$ is characterized by two effects: conduction and convection by the fluid phase, as expressed by the following equations:

$$f_{T,i} = -\lambda_{ij}\nabla_j T + c_{p,w} f_{w,i}(T - T_0) \tag{10}$$

where λ_{ij} is the mixture conductivity, and it depends on the thermal properties of the components. Notably, the convection of the solid phase is implicitly incorporated in the modelling through the updated Lagrangian formulation implemented in the LAGAMINE code (Charlier, 1987).

3.3. Constitutive law and material parameters

The classical Hooke's law is used to describe the linear elastic behaviour of Boom Clay, accounting for its transverse isotropy. For the plastic response, it is proposed to use an internal friction angle criterion such as a Drucker-Prager model (Drucker and Prager, 1952). For defining the onset of plastic yielding, the following yield criterion is adopted, which can be written as (positive in compression) (Desai and Siriwardane, 1984):

$$f \equiv \sqrt{II_{\hat{\sigma}}} - \frac{2\sin\phi}{\sqrt{3}\,(3-\sin\phi)}\left(I_\sigma + \frac{3c}{\tan\phi}\right) = 0 \tag{11}$$

where I_σ is the first stress tensor invariant defined by $I_\sigma = \sigma_{ii}$; $II_{\hat{\sigma}}$ is the second deviatoric stress tensor invariant defined by $II_{\hat{\sigma}} = \frac{1}{2}\widehat{\sigma}_{ij}\widehat{\sigma}_{ij}$ with $\hat{\sigma}_{ij} = \sigma_{ij} - \frac{I_\sigma}{3}\delta_{ij}$; ϕ and c are the internal friction angle and the cohesion.

A non-associated plastic flow rule is assumed with the plastic potential g corresponding to the function:

$$g \equiv \sqrt{II_{\hat{\sigma}}} - \frac{2\sin\psi}{\sqrt{3}\,(3-\sin\psi)}\left(I_\sigma + \frac{3c}{\tan\psi}\right) = 0 \tag{12}$$

where ψ is the dilatancy angle.

It is believed that the hardening and softening of the yield surface are induced by the plastic flow. By using the Von Mises equivalent plastic strain ϵ^p_{eq}, the variation of the yield surface is described by the hyperbolic evolution of friction angle and cohesion (Barnichon, 1998):

$$\phi = \phi_0 + \frac{(\phi_f - \phi_0)\,\epsilon^p_{eq}}{B_\phi + \epsilon^p_{eq}} \tag{13}$$

$$c = c_0 + \frac{(c_f - c_0)\epsilon^p_{eq}}{B_c + \epsilon^p_{eq}} \tag{14}$$

where ϕ_0 and ϕ_f are the initial and final friction angles, c_0 and c_f are the initial and final cohesion, and the coefficients B_ϕ and B_c are the values of the equivalent plastic strain where half of the hardening/softening of friction angle and cohesion are reached. The Von Mises equivalent plastic strain ϵ^p_{eq} is obtained by integration of the Von Mises equivalent plastic strain rate $\dot{\epsilon}^p_{eq}$:

$$\dot{\epsilon}^p_{eq} = \sqrt{\frac{2}{3}\dot{\hat{\epsilon}}^p_{eq}\dot{\hat{\epsilon}}^p_{eq}} \tag{15}$$

As a typical cross-anisotropic material, Boom Clay has higher THM parameters parallel to the bedding plane than those perpendicular to it. Tab. 4 defines the anisotropic material properties of Boom Clay which come mainly from Charlier et al. (2010), Bernier et al. (2007), and Chen et al. (2011). The elastic behavior is introduced by five independent parameters ($E_{\parallel}$, $E_{\perp}$, $\nu_{\parallel\parallel}$, $\nu_{\parallel\perp}$ and $G_{\parallel\perp}$), where the subscripts $\parallel$ and $\perp$ respectively represent the directions parallel and perpendicular to the bedding planes. The anisotropy of plasticity is taken into account through the cohesion, which is a function of a microstructure fabric tensor:

$$c_0 = \overline{c}\left(1 + A_{\parallel}(1 - 3l_2^2) + b_1 A_{\parallel}^2(1 - 3l_2^2)^2 + b_2 A_{\parallel}^3(1 - 3l_2^2)^3 + \cdots\right) \tag{16}$$

where $\overline{c}$ is the cohesion under isotropic loading, l_2 is the loading vector component applied to the facet parallel to the bedding planes. The constants $\overline{c}$, $A_{\parallel}$, b_1, ... are obtained from experimental data (François et al., 2014), and b_2 is neglected due to higher order terms. It should be noted that the value of cohesion depends on the loading direction l_2 as well as the fabric parameter $A_{\parallel}$. For this reason, a final value of cohesion c_f as one-third of the initial value c_0 is defined in this study to consider the cohesion softening. More details about the definition of fabric tensor can be found in Pietruszczak and Mroz (2000, 2001) and Chen et al. (2010).

Table 4: THM parameters for Boom Clay.

	Symbol	Name	Value	Unit
Elastic	ρ_s	Solid phase density	2639	kg/m^3
	$E_\parallel$	Young's modulus parallel to bedding	400	MPa
	$E_\perp$	Young's modulus normal to bedding	200	MPa
	$\nu_{\parallel\parallel}$	Poisson's ratio parallel to bedding	0.25	-
	$\nu_{\perp\parallel}$	Poisson's ratio normal to bedding	0.125	-
	$G_\perp$	Shear modulus normal to bedding	80	MPa
Plastic	ψ	Dilatancy angles	0	$^\circ$
	ϕ_0	Initial friction angle	5	$^\circ$
	ϕ_f	Final friction angle	18	$^\circ$
	B_ϕ	Friction angle hardening coefficient	0.01	-
	B_c	Cohesion softening coefficient	0.01	-
	$\overline{c}$	Cohesion for isotropic loading	258.33	kPa
	$A_\parallel$	Cohesion parameter	0.187	-
	b_1	Cohesion parameter	2.580	-
Hydraulic	$k_\parallel$	Intrinsic permeability parallel to bedding	4E-19	m^2
	$k_\perp$	Intrinsic permeability normal to bedding	2E-19	m^2
	ϕ	Porosity	0.39	-
	K_w^{-1}	Water compressibility	4.5E-4	MPa^{-1}
	ρ_w	Water density	1000	kg/m^3
Thermal	$c_{p,s}$	Solid phase specific heat	769	J/kg/K
	α_s	Linear thermal expansion coefficient	1E-5	K^{-1}
	$c_{p,w}$	Water specific heat	4180	J/kg/K
	$\lambda_\parallel$	Thermal conductivity parallel to bedding	1.65	W/m/K
	$\lambda_\perp$	Thermal conductivity normal to bedding	1.31	W/m/K

The concrete of the segmental lining is mainly made of C80/95 concrete. The concrete is modelled via a linear elastic law. As the ring is modelled without considering the existence of the joints (longitudinal and circumferential) between the concrete segments, a greater permeability than the Boom Clay is chosen as seen in Tab. 5.

Table 5: Concrete main properties.

Name	Symbol	Value	Unit
Solid phase density	ρ_s	2650	kg/m^3
Bulk density	ρ'	2420	kg/m^3
Porosity	n	0.1	
Young's modulus	E	42	GPa
Poisson's ratio	ν	0.2	–
Intrinsic permeability	k	4.5E-18	m^2
Thermal conductivity	λ	2.86	W/mK
Linear thermal expansion coefficient	α_s	1E-5	°C^{-1}
Solid phase specific heat	C_p	800	J/(kgK)

3.4. Numerical modelling results

As required by the PRACLAY benchmark exercise, the time evolution of temperature and pore pressure numerical prediction is compared to experimental measurement. The solid lines are the numerical results, and the dotted lines are the experimental measurements in the following plots. Generally, the reproduction of the temperature profile is almost perfect using the current modelling in Fig. 8. Ambient temperature is observed before the heating. As the heating phase is activated, the temperature increases rapidly, especially for the measurements close to the gallery wall. After the aimed temperature of 80 °C is reached, it keeps constant at the wall. With the distance between the wall and the measurements increases, a decrease in temperature is observed. To well capture the evolution of temperature, the thermal conductivity of the host clay formation is the most important parameter. In order to further improve the predictions, the horizontal thermal conductivity should slightly decrease and the vertical one slightly increase.

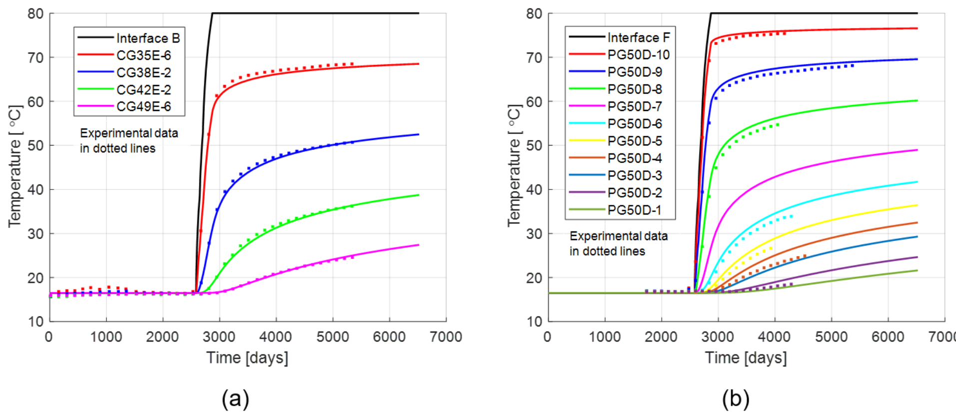

Figure 8: Temperature evolution: (a) in the horizontal, and (b) vertical directions.

In Fig. 9, the temporal evolution of the pore pressure at different sensors is presented. The deviation between the experimental measurements and numerical predictions is pronounced. Before the pressurization, the pore pressure decreases due to the drainage. An overestimation of the numerical prediction is observed in the horizontal direction. During the pressurization, pore pressure rises due to artificial injection. The numerical model consistently overestimates the pressure, and the deviation grows with an increasing distance between the wall and the measurement points. During the heating, pore pressure further increases. The overpressure is observed both in the near and far field due to the thermal pressurization, which is induced by the discrepancy of the thermal expansion between the solid and fluid phases. The numerical response underestimates the thermal pressurization. In the far field, the rock behavior remains elastic. According to the theoretical framework of thermo-poro-elasticity, the pore pressure variation is impacted by the modification of total stress and temperature, and it can be defined as follows considering material anisotropy:

$$dp = \Pi d\sigma + \Lambda dT \tag{17}$$

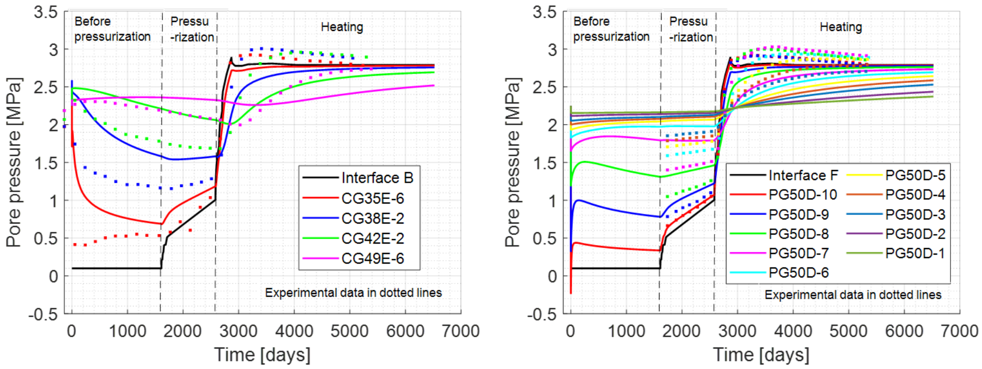

(a) (b)

Figure 9: The evolution of pore pressure: (a) in the horizontal, and (b) vertical directions (blank prediction).

Where Skempton's coefficient Π and thermal pressurization coefficient Λ have the following expressions:

$$
\begin{aligned}
\Pi &= \frac{-\boldsymbol{B} : \mathbb{C}}{\boldsymbol{B} : \mathbb{C}\boldsymbol{B} + \frac{1}{3K_s}(\boldsymbol{B} - \phi\boldsymbol{I}) : \boldsymbol{I} + \frac{\phi}{K_w}} \\
\Lambda &= \frac{3\phi(\alpha_l - \alpha_s)}{\boldsymbol{B} : \mathbb{C}\boldsymbol{B} + \frac{1}{3K_s}(\boldsymbol{B} - \phi\boldsymbol{I}) : \boldsymbol{I} + \frac{\phi}{K_w}}
\end{aligned} \tag{18}
$$

Where $\boldsymbol{B}$ is the Biot's coefficient tensor, $\mathbb{C}$ is the compliance tensor, $\boldsymbol{I}$ is the identity vector, K_s is the bulk modulus of the solid constituent, K_w is the bulk modulus of the fluid, ϕ is the porosity, α_l and α_s are the thermal expansion coefficients of the fluid phase and solid phase respectively. It is worth mentioning that the dependency of the thermal dilation coefficient and viscosity of the water on the temperature is also included in this study (Song et al., 2023). From the Eq. 18, the thermal pressurization coefficient Λ is not only affected by the discrepancy of thermal expansion coefficient between the fluid phase and solid phase but also by the stiffness of the porous medium (Vu et al., 2020). This is the reason why we propose to improve the elastic part of the model.

4. Advanced THM coupled modelling

The evolution of temperature was already well captured in section 3.4, herein the reproduction of pore pressure evolution is of particular interest. Pore pressure variations are fundamentally interconnected with the permeability characteristics of porous media. During the excavation, an EDZ is created in the near field where strain localization and damage occur. It has been shown that this damage induces the increase of permeability, both at the gallery scale (Mertens et al., 2004) and at the laboratory scale (Labiouse et al., 2014). This is why Chen et al. (2021a), Chen et al. (2021b), and Bumbieler et al. (2021) introduced two distinct zones (EDZ and sound layer) to model the in situ PRACLAY and ALC1604 heater tests, where a higher permeability value was employed in the EDZ. Moreover, the evolution of pore pressure is also impacted by the stiffness of porous media due to potential complex hydro-mechanical (HM) coupling effects. On the one hand, the geomaterials such as overconsolidated soil and clay rock exhibit strong non-linearity in the elastic domain (i.e. in the initial range of loading and during unloading and reloading), because the elastic moduli are strongly dependent on the mean effective stress (Hujeux, 1985). On the other hand, the Boom Clay stiffness shows a significant decrease with the deformation during the excavation of the Connecting Gallery, and the tangent stiffness at 0.01% deformation is approximately an order of magnitude larger than that at 1% deformation (Bernier et al., 2007). Thus a smaller clay stiffness was also considered in the EDZ in previous studies. In fact, whether to introduce a higher permeability or a lower material stiffness in the EDZ, the definition of the size of the EDZ is always challengeable in the numerical analyses. In this study, an alternative solution with the dependency of both the permeability and the clay stiffness on the mean effective stress and deformation is employed. The advanced THM model is able to predict both the permeability and elastic property evolution in the near and far field.

4.1. Theoretical framework

Modelling the mechanical and hydraulic property evolution inside the damage zone is an important concern when considering drainage and thermal pressurization in host rock/clay formation. The modification of permeability due to damage in the host rock/clay formation is related to the distribution of induced cracks, which might serve as preferential flow paths in the host rock/clay formation. The onset, development, accumulation, propagation, and coalescence of microcracks represent the damage caused by the microcracking process, which can be described by the shear strain accumulation in the numerical simulation. In this section, a strain-dependent isotropic evolution of the hydraulic permeability tensor is considered using a power (cubic) formulation (Pardoen et al., 2016), which reads:

$$k_{w,ij} = k_{w,ij,0} \left(1 + \beta_{per} \langle YI - YI^{thr} \rangle \hat{\varepsilon}_{eq}^{3}\right) \tag{19}$$

Where $k_{w,ij,0}$ is the initial intrinsic water permeability tensor, β_{per} is an evolution parameter, $\hat{\varepsilon}_{eq}$ is the Von Mises' equivalent deviatoric strain, YI is the yield index defined as the reduced second deviatoric stress invariant: $YI = II_{\hat{\sigma}}/II_{\hat{\sigma}}^{p}$, where $II_{\hat{\sigma}}^{p}$ is the second deviatoric stress invariant at plastic state. YI^{thr} represents the threshold value below which there is no intrinsic permeability variation. In the elastic state, YI is lower than 1, whereas YI is equal to 1 on the yield surface. The permeability increase is limited to a maximum of 1.5 times its initial value, which is back computed by considering the measurement of permeability of Boom Clay from the laboratory and in-situ (Bastiaens et al., 2006; Yu et al., 2013; Chen et al., 2021b). Furthermore, it should be mentioned that the increase in permeability is thought to be irreversible.

A strong non-linearity has been observed during the elastic loading and unloading processes, in which the clay stiffness plays a role (Callisto and Rampello, 2002). The dependency of clay stiffness on the stress path was defined by Laloui (1993), where the bulk modulus is characterised as a function of the mean effective stress $p' = I_{\sigma}/3$. As far as the Poisson's ratio remains constant in this study, the following expression for the elastic stiffness is obtained according to:

$$E = E_{ref} \left(\frac{p'}{p'_{ref}}\right)^{n^e} \tag{20}$$

Where E_{ref} is the Young's modulus at the referential mean effective stress p'_{ref}, n^e is the exponent to adapt different material properties. For numerical issues, the minimum value of p' is limited to 0.01 MPa. For some stiff clays, the stress-strain response may exhibit behavior closer to linear elasticity, while soft soils tend to show more logarithmic behavior.

Apart from the dependency on the stress path, the clay stiffness degradation is generally observed during underground excavation, where the clay stiffness is essentially controlled by the shear strain development. Three categories of strain levels are usually identified by Atkinson (1991): the very

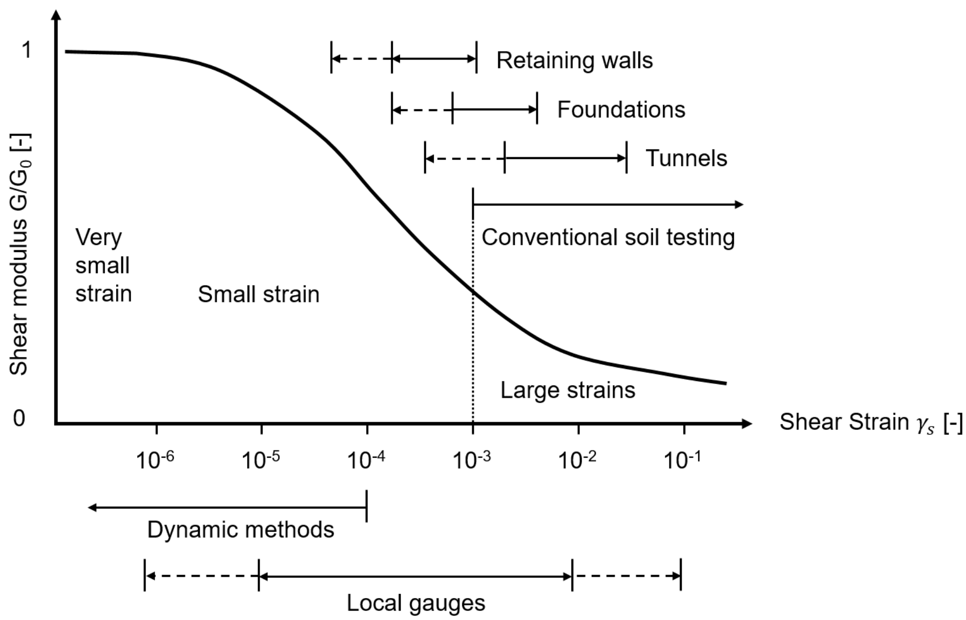

Figure 10: The logarithmic representation of stiffness-strain behavior according to Atkinson (1991).

small strain level, where the stiffness modulus remains constant within the range of elasticity; the small strain level, where the non-linear evolution of the stiffness modulus with the strain is presented; and the large strain level, where the soil stiffness is extremely small and the soil is close to failure. The normalized stiffness degradation curve, as depicted in Fig. 10, is used to illustrate this theory by comparison with the soil response from in situ construction and the measurement from the laboratory (Atkinson, 1991; Mair, 1993).

In order to introduce the dependency between the clay stiffness and deformation, a preliminary exponential model between Young's modulus and Von Mises strain was introduced in Chen et al. (2023), to model the degradation of clay stiffness from the far field to the near field. This approximation effectively captures the overall trend of pore pressure evolution. However, the calibration of multiple parameters introduces inherent inaccuracies, resulting in an underestimation of pore pressure in the near field and an overestimation in the far field. In this study, a more well-known constitutive law (HSsmall model) is further used to account for the evolution of stiffness at different strain levels (Brinkgreve et al., 2007; Benz et al., 2009). A logarithmic function of the shear strain γ, varying from extremely low strain levels to high strain levels, is used to represent the shear modulus G evolution (Likitlersuang et al., 2013). An empirical equation for tangent shear modulus depending on the shear strain is defined as (Hardin and Drnevich, 1972; Cudny and Truty, 2020):

$$G_t = \frac{G_0}{\left(1 + a\gamma_{max}/\gamma_{0.7}\right)^2} \tag{21}$$

where G_0 is the small-strain shear modulus, and many experimental results show its dependency on the void ratio, OCR, and mean stress (Hardin, 1978). The shear strain $\gamma_{0.7}$ corresponds to the shear strain at which the secant shear modulus is equal to 70% of G_0. The shear strain γ_{max} is the maximum deformation experienced by the sample. a is the evolution parameter. Due to the constant Poisson's ratio in this study, the evolution of Young's modulus is consistent with the shear modulus:

$$E_t = \frac{E_0}{\left(1 + a\gamma_{max}/\gamma_{0.7}\right)^2} \tag{22}$$

where E_0 corresponds to Young's modulus for a very small strain, and the value is very close to the one derived from the in situ wave velocities of seismic tests carried out in the underground repository (Schuster, 2019). Young's modulus will thus decrease with the development of shear strain from the initial E_0 where the sample is intact.

In this study, Young's modulus is influenced by the combined effects of both mean effective stress and shear strain deformation, so the parameters in Eq. 20 and Eq. 22 need to be calibrated. As shown in Tab. 4, the Young's moduli of Boom Clay (400/200 MPa in the directions parallel and normal to the bedding respectively) usually comes from the triaxial test with a referential confinement pressure of 2.25 MPa (ONDRAF/NIRAS, 2013), which is close to the in situ stress condition. In fact, the clay specimen is inevitably disturbed during the in situ sampling and the transportation between the in situ and the laboratory, thus higher Young's moduli are demonstrated for the intact clay materials. The in situ wave velocities of seismic tests provide these high moduli (1490/745 MPa) (Schuster, 2019), which is actually the E_0 in the Eq. 22 where the shear strain is very small. However, the in situ

Table 6: Parameters for the hydraulic permeability and small strain stiffness.

Symbol	Name	Value	Unit
$k_{w,0_{\parallel}}$	Intrinsic permeability parallel to bedding	4E-19	m^2
$k_{w,0_{\perp}}$	Intrinsic permeability normal to bedding	2E-19	m^2
β_{per}	Evolution parameter	1.5E5	–
YI^{thr}	threshold yield index	0.95	–
$E_{ref_{\parallel}}$	Referential Young's modulus parallel to bedding	1600	MPa
$E_{ref_{\perp}}$	Referential Young's modulus normal to bedding	800	MPa
p'_{ref}	Referential mean effective stress	2.25	MPa
n^e	Evolution parameter	0.4	–
$\gamma_{0.7}$	Evolution parameter	0.012	–
a	Evolution parameter	0.385	–

stress condition for Boom Clay is anisotropic, the referential Young's moduli under 2.25 MPa confinement needs to be back computed using the Eq. 20, yielding values of 1600/800 MPa. The parameters used in the modelling are summarized in Tab. 6, and they are also consistent with Chen et al. (2023), Pardoen et al. (2016), and the EURAD benchmark specification.

4.2. Laboratory test modelling

An advanced THM coupled modelling has been introduced in section 4.1, where the dependency of Young's modulus on the confining stress and shear deformation is highlighted. Calibration of numerical models for geomaterials is typically performed by simulating laboratory triaxial tests, which focuses primarily on the rock behavior during shear processes. In this study, a more comprehensive approach is adopted, modelling the entire process from in situ sample extraction to laboratory testing. The objectives of this modelling are twofold: first, to verify the reliability of the Young's modulus obtained from seismic test, which estimates the intact clay properties in the far field; and secondly, to ensure that the model accurately predicts the Young's modulus measured in the laboratory.

A simplified 2D axisymmetric model with one isoparametric element (section 3.1) is introduced to restore the procedure of measuring Young's modulus in the laboratory. The plastic behavior is governed by the Drucker–Prager criterion with isotropic hardening/softening. This modelling is composed of three sequential steps: on-site sampling, isotropic confinement, and deviatoric loading, each defined by specific boundary conditions. The release of in situ stress is first modelled to reproduce the extraction of samples from drilling boreholes. Considering the excavation rate, the clay formation far away from the gallery is supposed to be in undrained condition, so only the total stress decreases to zero in the first step. The sample is then delivered to the laboratory in preparation for the triaxial compression test. In the second step, an isotropic confining stress of 4.5 MPa is imposed to restore the in situ stress state of the clay formation, and the pore pressure is set to the in situ value of 2.25 MPa. Finally, the shear process is modelled using the strain-controlled deformation of the sample. The unloading/reloading path is also modelled during the shear process, to highlight the degradation of Young's modulus. The final amount of sample deformation is nearly 5%. The parameters used in this modelling are already provided in Tab. 6. The results confirm the potential perturbations induced by sampling and transportation processes on the evolution of Young's modulus.

Fig. 11 shows the comparison of stress-strain relation during the shear process with experimental test from Baldi et al. (1991) and Monfared (2011). When the sample is first loaded, an elastic deformation develops before the plastic deformation. Two unloading/reloading paths are introduced during the shear process, and the value of Young's modulus is deduced from the slope of the unloading path where the material is in elasticity. At the beginning of shear phase, the value of Young's modulus is slightly lower than the initial $E_{ref_\perp} = 800$ MPa due to a small amount of shear deformation induced by its inherent anisotropic behavior in the first and second steps. The numerical solution overestimates the Young's modulus compared to the experimental results, which should come from the potential disturbance during sampling and transportation.

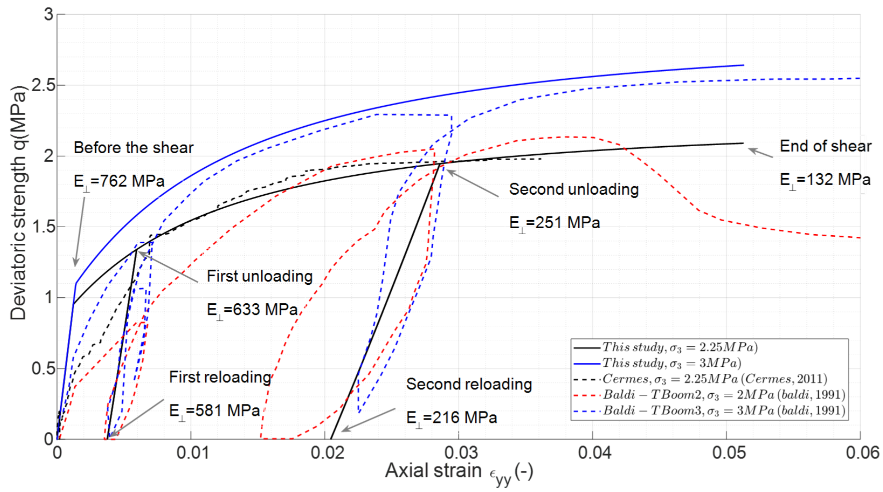

Figure 11: Stress-strain curve during the shear process of the triaxial test.

During the shearing process, the degradation of Young's modulus with the shear deformation is highly pronounced, although the mean effective stress has been increasing. The impact of mean effective stress on the evolution of Young's modulus is more clearly observed during unloading and reloading, as the variation of Young's modulus is no longer influenced by shear deformation in these stages. It is worth mentioning that Young's modulus is defined as a function of the maximum shear deformation experienced by the sample, which is consistent with the irreversibility of damage observed in experimental tests. Overall, the degradation of the stiffness of the material is first induced by the inevitable disturbance from the on-site sampling but mostly by the imposed strain amplitude during the triaxial test. The measurement of the Young's modulus in the laboratory is around 200 MPa, which corresponds to the numerical prediction within several percent deformation in Fig. 11. The implemented modelling is able to capture the shear strength obtained from the experimental tests. It should be mentioned that, the shear strength of the sample is not only impacted by the strength parameters but also the confining pressure. Another modelling is conducted with confinement of 3 MPa, where a good agreement is obtained between the numerical and experimental observations.

4.3. Application to PRACLAY heater test

The advanced THM coupled modelling has been successfully calibrated with small scale laboratory test in section 4.2. The degradation of Young's modulus has been accurately reproduced and the modulus in the far field has been confirmed. It is now of particular interest to extend this modelling to the in situ large-scale PRACLAY heater test. Before simulating the evolution of pore pressure, it is essential to examine excavation-induced plasticity as a methodology of further validating the implemented constitutive model. Fig. 12 displays the post-excavation contour plots, illustrating the distributions of stress, permeability, and equivalent shear strain. At the end of the excavation (t_0+1 day), contact between the gallery wall and the concrete liner is established nearly everywhere, except in the vertical direction (Fig. 12a). Stress redistribution due to excavation is clearly observed in both the horizontal and vertical directions (Figs. 12b and c), where the different contact situation between the gallery wall and the liner also plays an important role on the observed stress patterns. A significant increase in permeability is detected within the EDZ (Figs. 12d and e), with maximum values reaching approximately 1.5 times the initial permeability. The maximum values of equivalent shear strain are found near the vertical direction (Fig. 12f), corresponding to the region where the contact between the gallery wall and the liner is weakest.

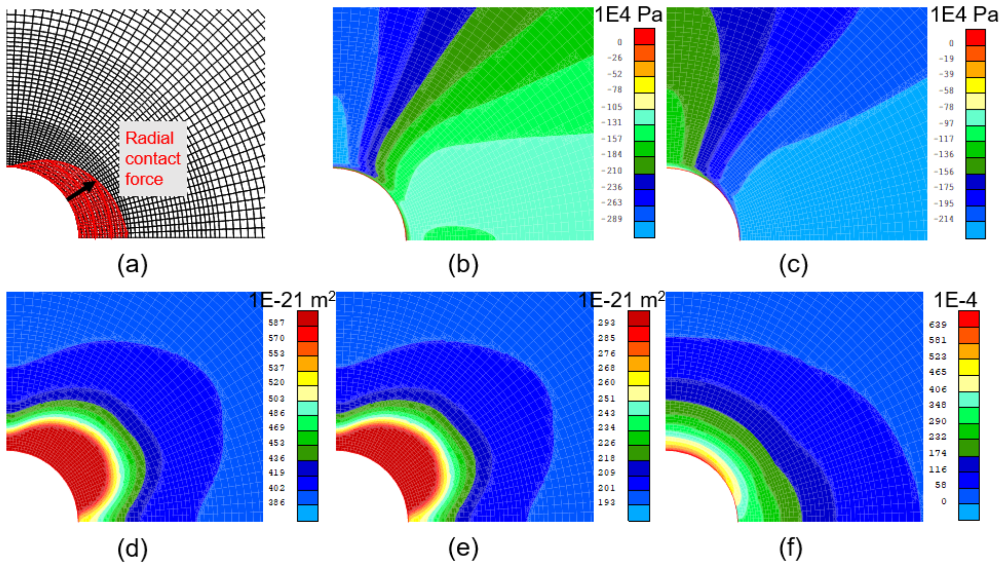

Figure 12: Post-excavation contour at t_0+1 day in 4 m × 4 m scale: (a) contact force, (b) horizontal stress σ_{xx}, (c) vertical stress σ_{yy}, (d) horizontal permeability k_{xx}, (e) vertical permeability k_{yy}, (f) equivalent shear strain.

Fig. 13 shows the pore pressure evolution with the implemented model. During the drainage and injection phases, the pore pressure is successfully captured in the near field in both directions. However, the experimental results are not so well reproduced in the far field during the injection phase, where the pore pressure is still overestimated at the measurements PG50D-6, PG50D-5, and PG50D-4. The good prediction of pressure in the near field has to be related to the evolution of the permeability. The plastic deformation is much developed due to the excavation, leading to the creation of an EDZ with higher permeability. Fig. 14 depicts the evolution of permeability in the horizontal and vertical directions. The estimated impacted zone of the permeability variation is around 4 m from the gallery axis. The maximum increase of the permeability is located close to the gallery wall, and it is about 1.5 times than the initial value in the end of heating. The modification of permeability is more pronounced in the vertical direction, which is consistent with the distinct development of the equivalent shear strain in Fig. 15. The deformation inside the EDZ in the vertical direction is greater than that in the horizontal direction, which is consistent with the 'eye shape' of EDZ in Salehnia et al. (2015) and François et al. (2014). The shear strain localization is preferential to develop in the minor principal stress direction.

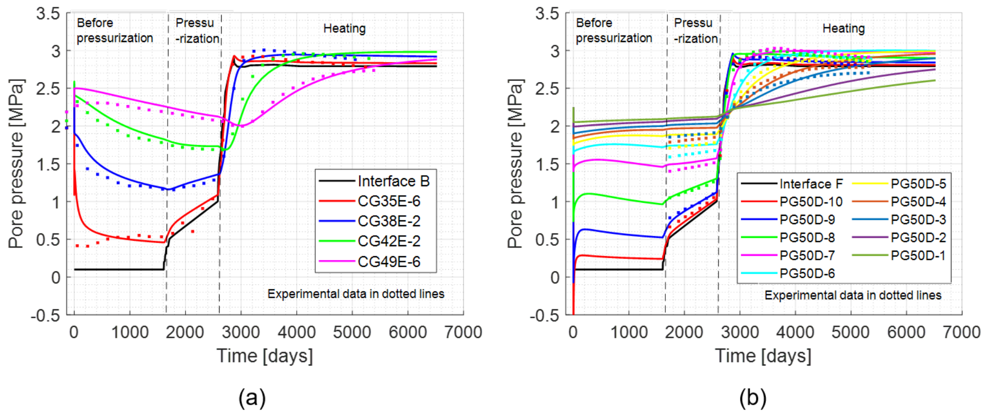

Figure 13: The evolution of pore pressure: (a) in the horizontal, and (b) vertical directions.

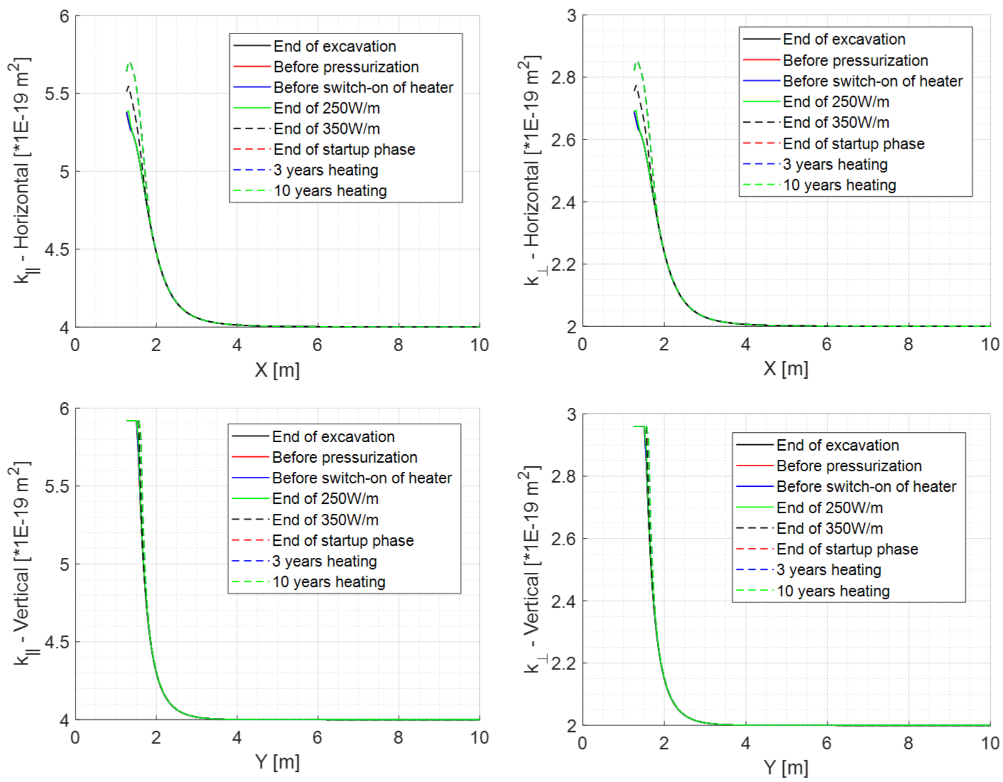

Figure 14: The variation of Permeability in the horizontal and vertical directions.

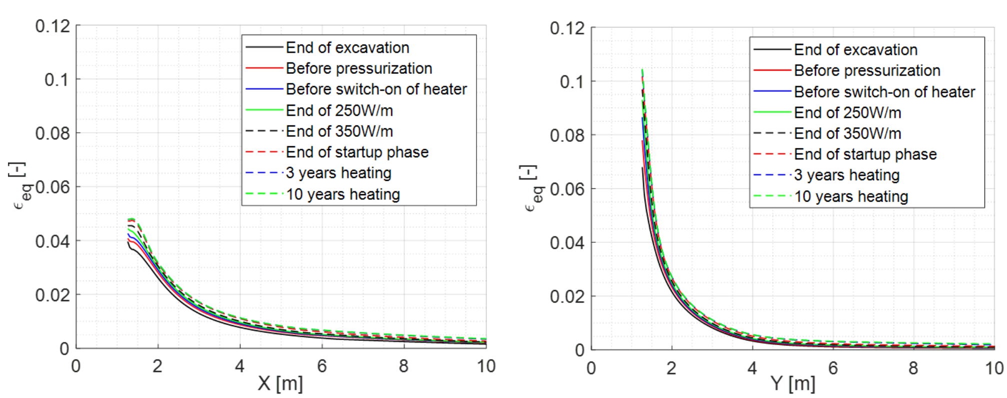

Figure 15: The evolution of equivalent shear strain in the horizontal and vertical directions.

The overpressure induced by thermal pressurization is well reproduced both in the near and far field during the heating, where the THM coupling is magnified thanks to the higher clay stiffness. Fig. 16 characterizes the variation of Young's modulus in the horizontal and vertical directions. Globally, a significant decrease of Young's modulus is observed from the far field to the wall, and the minimum values are obtained at the wall in the end of heating. This relates to the fact that deformation plays a dominant role in the evolution of Young's modulus. For the clay formation very close to the wall, the degradation of the clay stiffness is consistent between the excavation and heating phase, because most of the shear deformation is induced by the excavation of the gallery. The Young's modulus remains constant in the far field, where the clay formation is almost intact. In the direction parallel to the bedding, a value higher than the initial modulus is observed in the clay formation slightly further from the wall, reflecting the dependency of clay stiffness on mean effective stress. Fig. 17 displays the evolution of the mean effective stress, where the peak stress in the bedding plane coincide with the peak modulus in Fig. 16, and a larger modulus than the intact one (1490 MPa) is observed at a distance of 10 m from the wall. The peak stress in the direction normal to the bedding occurs extremely close to the wall where the minimum modulus is obtained, which again evidences the dominance of deformation in the evolution of Young's modulus in the EDZ.

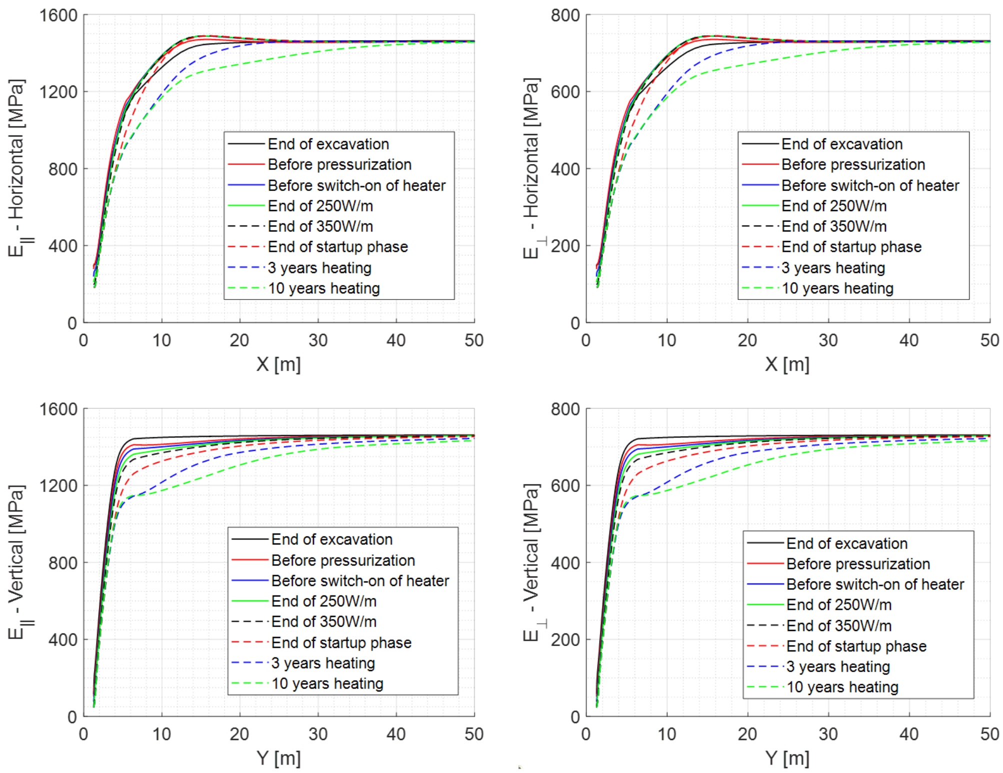

Figure 16: The variation of Young's modulus in the horizontal and vertical directions.

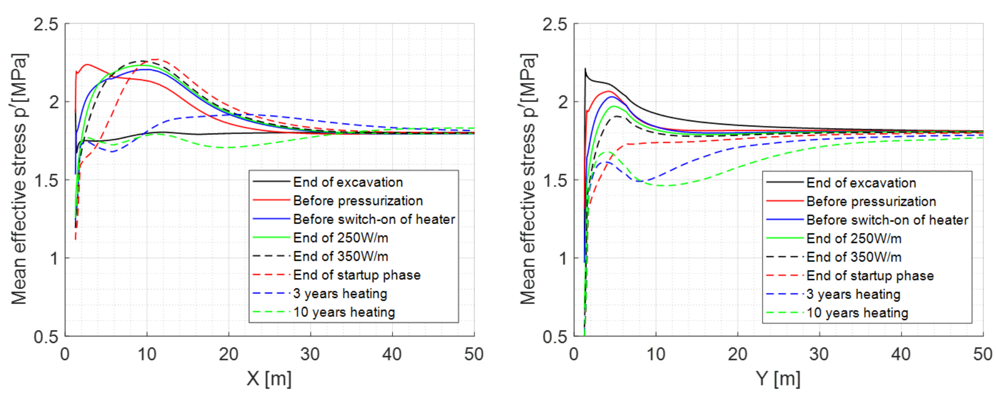

Figure 17: The evolution of mean effective stress in the horizontal and vertical directions.

It is worth mentioning that, the numerical prediction is unable to capture the decrease in pore pressure displayed at the end of heating. This deviation is related to the 3D effect in the real repository, which is out of the scope of the 2D modelling problem in this study. The results show that the extent of the zone with permeability changes is much smaller than the zone with clay stiffness modification. The impacted zone of Young's modulus in the horizontal direction is larger than in the vertical direction.

5. Conclusion

A large-scale in situ PRACLAY heater test is currently being carried out at HADES URL to analyze the thermal impacts in the EDZ (or the near field) and to confirm the far-field response. A 2D benchmark is proposed to represent the PRACLAY heater test using fully coupled THM finite element codes. The thermal pressurization mechanism is recalled in this study, which shows that the excess pore pressure during the heating is not only related to the discrepancy of thermal expansion coefficient between fluid and solid phase but also to the material stiffness. The comparison between the numerical prediction and experimental observation is carried out.

The evolution of temperature is well captured compared to the in situ measurement. To reproduce the evolution of pore pressure, an advanced constitutive model is implemented by integrating the strain dependency of the clay stiffness and intrinsic permeability of the host clay formation, and the HSsmall model into the numerical predictions. A laboratory test modelling from the in situ extraction of the sample to the triaxial test is carried out, to verify that the advanced model is able to predict stiffness changes from field to laboratory conditions. The degradation of the clay stiffness is reproduced, and the in situ clay modulus in the far field is confirmed. The degradation of Young's modulus is first induced by the inevitable disturbance from the on-site sampling but mostly by the strain amplitude during the triaxial test. In the end, the implemented modelling is able to capture the shear strength from the experimental tests and the Young's modulus commonly measured in the lab.

A good agreement between the numerical prediction and in situ measurement is obtained after the application of the advanced model. The increase of intrinsic permeability and the degradation of Young's modulus are strongly dependent on the development of shear strain deformation, which appears mostly during the excavation of the gallery. The pore pressure during the drainage is reproduced thanks to the introduction of permeability increase in the EDZ (near field). The THM coupling during the heating is magnified by the combined effect from the mean effective stress and shear deformation, thus the excess pore pressure is well captured. Specially, the combined effect of the mean effective stress and shear deformation on the Young's modulus is investigated in this study. The shear deformation dominates the development of the Young's modulus, and the impact from the mean effective stress is evidenced, where the shear deformation is smaller in the direction parallel to the bedding plane. In addition, the impacted zone of the Young's modulus between the horizontal and vertical directions is consistent with the in situ 'eye shape' damage zone. The extent of the zone with permeability changes is much smaller than the zone with clay stiffness modification. It is worth mentioning that, the effects of temperature on thermal compaction, creep behavior, and potential strength modification of the rock are not included in this study.

CRediT authorship contribution statement

Hangbiao Song: Conceptualization, investigation, methodology, software, validation, writing - original draft. Arnaud Dizier: Conceptualization, investigation, writing – review and editing. Séverine Levasseur: Conceptualization, investigation, writing – review and editing. Suresh Seetharam: Conceptualization, investigation, validation. Frédéric Collin: Conceptualization, investigation, methodology, project administration, writing - review and editing.

Declarations

The authors declare that they have no known competing financial interests or personal relationships that could have appeared to influence the work reported in this paper.

Acknowledgments

This project has received funding from the European Union's Horizon 2020 research and innovation programme under grant agreement No 847593. The first author also would like to thank the China Scholarship Council (No.201906710096) for their financial support.

Data availability

No data was used for the research described in the article.

References

Armand, G., Bumbieler, F., Conil, N., de La Vaissière, R., Bosgiraud, J.M., Vu, M.N., 2017. Main outcomes from in situ thermo-hydro-mechanical experiments programme to demonstrate feasibility of radioactive high-level waste disposal in the callovo-oxfordian claystone. J. Rock Mech. Geotech. Eng. 9, 415–427.

Atkinson, J., 1991. Experimental determination of stress-strain-time characteristics in laboratory and-in-situ tests. general report, in: Proc. 10th Eur. Conf. Soil Mech. Found. Eng., pp. 915–956.

Baldi, G., Hueckel, T., Peano, A., Pellegrini, R., 1991. Developments in modelling of thermohydro-geomechanical behaviour of Boom clay and clay-based buffer materials (volume 2). Technical Report. Commission of the European Communities.

Baldi, G., Hueckel, T., Pellegrini, R., 1988. Thermal volume changes of the mineral–water system in low-porosity clay soils. Can. Geotech. J. 25, 807–825.

Barnichon, J.D., 1998. Finite element modelling in structural and petroleum geology. Ph.D. thesis. Universite de Liège.

Bastiaens, W., Bernier, F., Li, X., 2006. An overview of long-term hm measurements around hades urf, in: Proc. EUROCK, pp. 9–12.

Benz, T., Schwab, R., Vermeer, P., 2009. Small-strain stiffness in geotechnical analyses. Bautechnik 86, 16–27.

Bernier, F., Li, X., Bastiaens, W., 2007. Twenty-five years' geotechnical observation and testing in the tertiary boom clay formation. Géotechnique 57, 229–237.

Bernier, F., Neerdael, B., 1996. Overview of in-situ thermomechanical experiments in clay: Concept, results and interpretation. Eng. Geol. 41, 51–64.

Bossart, P., Meier, P.M., Moeri, A., Trick, T., Mayor, J.C., 2002. Geological and hydraulic characterisation of the excavation disturbed zone in the opalinus clay of the mont terri rock laboratory. Eng. Geol. 66, 19–38.

Braun, P., Delage, P., Ghabezloo, S., Chabot, B., Conil, N., Vu, M.N., 2022. Inducing tensile failure of claystone through thermal pressurization in a novel triaxial device. Rock Mech. Rock Eng. 55, 3881–3899.

Bredehoeft, J.D., 1978. Geologic disposal of high-level radioactive wastes: Earth-science perspectives. volume 779. US Department of the Interior, Geological Survey.

Brinkgreve, R., Kappert, M., Bonnier, P., 2007. Hysteretic damping in a small-strain stiffness model. Proc. Num. Mod. Geomech., NUMOG X, Rhodes , 737–742.

Bumbieler, F., Plúa, C., Tourchi, S., Vu, M.N., Vaunat, J., Gens, A., Armand, G., 2021. Feasibility of constructing a full-scale radioactive high-level waste disposal cell and characterization of its thermo-hydro-mechanical behavior. Int. J. Rock Mech. Min. 137, 104555.

Callisto, L., Rampello, S., 2002. Shear strength and small-strain stiffness of a natural clay under general stress conditions. Géotechnique 52, 547–560.

Charlier, R., 1987. Approche unifiee de quelques problemes non lineaires de mecanique des milieux continus par la methode des elements finis. Ph.D. thesis.

Charlier, R., Chambon, R., Collin, F., Dedecker, F., Dizier, A., Fauriel, S., François, B., Fokkens, J., Garitte, B., Gens, A., et al., 2010. Deliverable d13–simulation of lab and in situ tests. Timodaz Rep. .

Chen, G., Dizier, A., Li, X., Verstricht, J., Sillen, X., Levasseur, S., 2021a. Numerical prediction of the large-scale in situ praclay heater test in the boom clay. Rock Mech. Rock Eng. 54, 2197–2218.

Chen, G., Dizier, A., Verstricht, J., Li, X., 2021b. Scientific interpretation of the first years of the praclay heater test. EURIDICE Rep. EUR_20-058 .

Chen, G., Li, X., Dizier, A., Verstricht, J., Sillen, X., Levasseur, S., 2023. Characterization of boom clay anisotropic thm behaviour based on two heating tests at different scales in the hades url. Geol. Soc., Lond. Spec. Publ. 536, SP536–2022.

Chen, G., Sillen, X., Verstricht, J., Li, X., 2011. Atlas iii in situ heating test in boom clay: Field data, observation and interpretation. Comput. Geotech. 38, 683–696.

Chen, L., Shao, J.F., Huang, H., 2010. Coupled elastoplastic damage modeling of anisotropic rocks. Comput. Geotech. 37, 187–194.

Collin, F., Li, X.L., Radu, J.P., Charlier, R., 2002. Thermo-hydro-mechanical coupling in clay barriers. Eng. Geol. 64, 179–193.

Conil, N., Vitel, M., Plua, C., Vu, M.N., Seyedi, D., Armand, G., 2020. In situ investigation of the thm behavior of the callovo-oxfordian claystone. Rock Mech. Rock Eng. 53, 2747–2769.

Croisé, J., Schlickenrieder, L., Marschall, P., Boisson, J., Vogel, P., Yamamoto, S., 2004. Hydrogeological investigations in a low permeability claystone formation: the mont terri rock laboratory. Phys. Chem. Earth (Pt AB,C) 29, 3–15.

Cudny, M., Truty, A., 2020. Refinement of the hardening soil model within the small strain range. Acta Geotech. 15, 2031–2051.

Cui, Y.J., Le, T.T., Tang, A.M., Delage, P., Li, X.L., 2009. Investigating the time-dependent behaviour of boom clay under thermomechanical loading. Géotechnique 59, 319–329.

Cui, Y.J., Sultan, N., Delage, P., 2000. A thermomechanical model for saturated clays. Can. Geotech. J. 37, 607–620.

Dao, L.Q., Cui, Y.J., Tang, A.M., Pereira, J.M., Li, X.L., Sillen, X., 2015. Impact of excavation damage on the thermo-hydro-mechanical properties of natural boom clay. Eng. Geol. 195, 196–205.

De Bruyn, D., Labat, S., 2002. The second phase of atlas: the continuation of a running thm test in the hades underground research facility at mol. Eng. Geol. 64, 309–316.

Delage, P., Sultan, N., Cui, Y.J., 2000. On the thermal consolidation of boom clay. Can. Geotech. J. 37, 343–354.

Desai, C.S., Siriwardane, H.J., 1984. Constitutive laws for engineering materials, with emphasis on geologic materials. Prentice-Hall.

Dizier, A., Chen, G., Li, X., Leysen, J., Verstricht, J., Troullinos, I., Rypens, J., 2016. The start-up phase of the praclay heater test. EUR_PH_16_025. Mol, Belgium .

Dizier, A., Chen, G., Verstricht, J., Li, X., Sillen, X., Levasseur, S., 2021. The large-scale in situ praclay heater test: first observations on the in situ thermo-hydro-mechanical behaviour of boom clay. Int. J. Rock Mech. Min. 137, 104558.

Drucker, D.C., Prager, W., 1952. Soil mechanics and plastic analysis or limit design. Q. Appl. Math. 10, 157–165.

EURAD-HITEC, 2019. EURAD WP HITEC Milestone report 49 – Selection of benchmark exercises for task 2.3. Technical Report.

Félix, B., Lebon, P., Miguez, R., Plas, F., 1996. A review of the andra's research programmes on the thermo-hydromechanical behavior of clay in connection with the radioactive waste disposal project in deep geological formations. Eng. Geol. 41, 35–50.

François, B., Labiouse, V., Dizier, A., Marinelli, F., Charlier, R., Collin, F., 2014. Hollow cylinder tests on boom clay: modelling of strain localization in the anisotropic excavation damaged zone. Rock Mech. Rock Eng. 47, 71–86.

Garitte, B., Nguyen, T., Barnichon, J., Graupner, B., Lee, C., Maekawa, K., Manepally, C., Ofoegbu, G., Dasgupta, B., Fedors, R., et al., 2017. Modelling the mont terri he-d experiment for the thermal–hydraulic–mechanical response of a bedded argillaceous formation to heating. Environ. Earth Sci. 76, 1–20.

Gens, A., Vaunat, J., Garitte, B., Wileveau, Y., 2011. In situ behaviour of a stiff layered clay subject to thermal loading: observations and interpretation, in: Stiff Sedimentary Clays: Genesis and Engineering Behaviour: Géotechnique Symposium in Print 2007, Thomas Telford Ltd. pp. 123–144.

Gens Solé, A., Barboza de Vasconcelos, R., Olivella Pastallé, S., 2020. Towards higher temperatures in nuclear waste repositories, in: E3S Web Conf., EDP Sciences. pp. 1–8.

Ghabezloo, S., Sulem, J., Saint-Marc, J., 2009. The effect of undrained heating on a fluid-saturated hardened cement paste. Cement Concrete Res. 39, 54–64.

Hardin, B.O., 1978. The nature of stress-strain behavior for soils, in: From Volume I of Earthquake Engineering and Soil Dynamics–Proceedings of the ASCE Geotechnical Engineering Division Specialty Conference, June 19-21, 1978, Pasadena, California. Sponsored by Geotechnical Engineering Division of ASCE in cooperation with:.

Hardin, B.O., Drnevich, V.P., 1972. Shear modulus and damping in soils: design equations and curves. J. Soil Mech. Found. Division 98, 667–692.

Hujeux, J.C., 1985. Une loi de comportement pour le chargement cyclique des sols, in: Génie parasismique, pp. 287–302.

IAEA, 2003. Scientific and technical basis for the geological disposal of radioactive wastes. Number 413 in Tech. Rep. Ser., International Atomic Energy Agency.

IAEA, 2022. Status and trends in spent fuel and radioactive waste management. Number NW-T-1.14 (Rev. 1) in Nucl. Energy Ser., International Atomic Energy Agency.

Kell, G.S., 1975. Density, thermal expansivity, and compressibility of liquid water from 0. deg. to 150. deg.. correlations and tables for atmospheric pressure and saturation reviewed and expressed on 1968 temperature scale. J. Chem. Eng. Data 20, 97–105.

Labiouse, V., Sauthier, C., You, S., 2014. Hollow cylinder simulation experiments of galleries in boom clay formation. Rock Mech. Rock Eng. 47, 43–55.

Laloui, L., 1993. Modélisation du comportement thermo-hydro-mécanique des milieux poreux anélastiques. Ph.D. thesis. Ecole Centrale Paris.

Li, X., Bastiaens, W., Van Marcke, P., Verstricht, J., Chen, G., Weetjens, E., Sillen, X., 2010. Design and development of large-scale in-situ praclay heater test and horizontal high-level radioactive waste disposal gallery seal test in belgian hades. J. Rock Mech. Geotech. Eng. 2, 103–110.

Li, X., Dizier, A., Chen, G., Verstricht, J., Levasseur, S., 2023a. Forty years of investigation into the thermo-hydromechanical behaviour of boom clay in the hades url .

Li, X., Neerdael, B., Raymaekers, D., Sillen, X., 2023b. The construction of the hades underground research laboratory and its role in the development of the belgian concept of a deep geological repository. Geol. Soc., Lond. Spec. Publ. 536, SP536–2022.

Likitlersuang, S., Teachavorasinskun, S., Surarak, C., Oh, E., Balasubramaniam, A., 2013. Small strain stiffness and stiffness degradation curve of bangkok clays. Soils Found. 53, 498–509.

Mair, R., 1993. Developments in geotechnical engineering research: application to tunnels and deep excavations, in: Proc. Inst. Civ. Engrs. Civ. Eng., pp. 27–41.

Mertens, J., Bastiaens, W., Dehandschutter, B., 2004. Characterisation of induced discontinuities in the boom clay around the underground excavations (urf, mol, belgium). Appl. Clay Sci. 26, 413–428.

Monfared, M., 2011. Couplages température-endommagement-perméabilité dans les sols et les roches argileux. Ph.D. thesis. Université Paris-Est.

Müller, H.R., Garitte, B., Vogt, T., Köhler, S., Sakaki, T., Weber, H., Spillmann, T., Hertrich, M., Becker, J.K., Giroud, N., et al., 2018. Implementation of the full-scale emplacement (fe) experiment at the mont terri rock laboratory. Mont Terri Rock Laboratory, 20 Years: Two Decades of Research and Experimentation on Claystones for Geological Disposal of Radioactive Waste , 289–308.

Neerdael, B., Boyazis, J., 1997. The belgium underground research facility: Status on the demonstration issues for radioactive waste disposal in clay. Nucl. Eng. Des. 176, 89–96.

ONDRAF/NIRAS, R.N.T...E., 2013. Development and Demonstration Plan for the geological disposal of high-level and/or long-lived radioactive waste including irradiated fuel if considered as waste, State-of-the-art report as of December 2012. Technical Report.

Pardoen, B., Talandier, J., Collin, F., 2016. Permeability evolution and water transfer in the excavation damaged zone of a ventilated gallery. Int. J. Rock Mech. Min. 85, 192–208.

Pietruszczak, S., Mroz, Z., 2000. Formulation of anisotropic failure criteria incorporating a microstructure tensor. Comput. Geotech. 26, 105–112.

Pietruszczak, S., Mroz, Z., 2001. On failure criteria for anisotropic cohesive-frictional materials. Int. J. Number. Anal. Met. 25, 509–524.

Plúa, C., Vu, M.N., Seyedi, D.M., Armand, G., 2021. Effects of inherent spatial variability of rock properties on the thermo-hydro-mechanical responses of a high-level radioactive waste repository. Int. J. Rock Mech. Min. 145, 104682.

Rumble, J., 2019. Crc handbook of chemistry and physics (100th ed.). boca rotan, fl.

Salehnia, F., Collin, F., Li, X.L., Dizier, A., Sillen, X., Charlier, R., 2015. Coupled modeling of excavation damaged zone in boom clay: Strain localization in rock and distribution of contact pressure on the gallery's lining. Comput. Geotech. 69, 396–410.

Schuster, K., 2019. Mini-seismic methods for the in-situ characterization of clay rocks—examples from url meuse/haute-marne (france) and hades urf (belgium). Geomech. Energy Envir. 17, 16–28.

Seyedi, D., Plúa, C., Vitel, M., Armand, G., Rutqvist, J., Birkholzer, J., Xu, H., Guo, R., Thatcher, K., Bond, A., et al., 2021. Upscaling thm modeling from small-scale to full-scale in-situ experiments in the callovo-oxfordian claystone. Int. J. Rock Mech. Min. 144, 104582.

Simo, E., de Lesquen, C., Leon-Vargas, R.P., Vu, M.n., Raude, S., El Tabbal, G., Dizier, A., Seetharam, S., Narkuniene, A., Collin, F., et al., 2025. Thm-modelling benchmark initiative on the effects of temperature on the disposal of heat-generating radioactive waste in clay formations. Acta Geotech. , 1–22.

Sojoudi, M., Li, B., 2023. A thermodynamic-based model for modeling thermo-elastoplastic behaviors of saturated clayey soils considering bound water dehydration. J. Rock Mech. Geotech. Eng. 15, 1535–1546.

Sojoudi, M., Li, B., Norouzi, E., 2024. Thermal-hydro-mechanical modeling of short-term ground responses due to the borehole thermal energy storage operations in a canadian subarctic region. Renew. Energ. 229, 120753.

Song, H., Corman, G., Collin, F., 2023. Thermal impact on the excavation damage zone around a supported drift using the 2nd gradient model. Rock Mech. Rock Eng. 56, 7575–7598.

Sultan, N., Cui, Y.J., Delage, P., 2010. Yielding and plastic behaviour of boom clay. Géotechnique 60, 657–666.

Sultan, N., Delage, P., Cui, Y., 2002. Temperature effects on the volume change behaviour of boom clay. Eng. Geol. 64, 135–145.

Van Marcke, P., Li, X., Bastiaens, W., Verstricht, J., Chen, G., Leysen, J., Rypens, J., 2013. The design and installation of the praclay in-situ experiment. EURIDICE Rep. , 13–129.

Vu, M.N., Armand, G., Plua, C., 2020. Thermal pressurization coefficient of anisotropic elastic porous media. Rock Mech. Rock Eng. 53, 2027–2031.

Yu, L., Rogiers, B., Gedeon, M., Marivoet, J., De Craen, M., Mallants, D., 2013. A critical review of laboratory and in-situ hydraulic conductivity measurements for the boom clay in belgium. Appl. Clay Sci. 75, 1–12.